Enhanced particle confinement and turbulence reduction due to $\boldsymbol{E} \times \boldsymbol{B}$ shear in the TEXTOR tokamak

J. Boedo[a], D. Gray[a], S. Jachmich[b], R. Conn[a], G.P. Terry[c], G. Tynan[a], G. Van Oost[b], R.R. Weynants[b], TEXTOR Team[d]

[a] Department of Aerospace and Mechanical Engineering, Fusion Energy Research Program, University of California, San Diego, California, United States of America

[b] Laboratoire de Physique des Plasmas/Laboratorium voor Plasmafysica, Association Euratom–Belgian State, École Royale Militaire/Koninklijke Militaire School, Brussels, Belgium

[c] Department of Physics, University of Wisconsin-Madison, Madison, Wisconsin, United States of America

[d] Institut für Plasmaphysik, Forschungzentrum Jülich GmbH, Association Euratom–Forschungzentrum Jülich, Jülich, Germany

Abstract. Positive radial electric fields have been created at the edge of the TEXTOR tokamak plasma using an electrode. The electric field induces a thin ($\delta r \sim 1.5$ cm), $\boldsymbol{E} \times \boldsymbol{B}$ driven layer at the edge rotating poloidally at 12–20 km/s and featuring high shear. Concomitant changes in the density and poloidal electric field fluctuations and their cross-phase in the shear layer result in suppression of radial turbulent particle transport, even at low radial electric field strength. Temperature fluctuations are reduced, resulting in diminished turbulent heat flux. As turbulent particle transport is quenched, the particle confinement time τ_p increases by a factor of 2 and the energy confinement time τ_E by 20%. Turbulent transport accounts for ∼50% of the total particle flux. Both the cross-phase and the density fluctuations are sensitive to the sign of ∇E_r.

1. Introduction

Tokamak plasmas can undergo transitions from a low energy confinement state (L mode) to a higher energy confinement state [1] (H mode) spontaneously. The transition is accompanied by a negative radial electric field inside the LCFS and is characterized by a steepening of the edge profiles, or formation of a transport barrier, and a fast reduction of the H_α signal, corresponding to increased particle confinement. Similar behaviour to the spontaneous L–H transition was obtained in the CCT tokamak [2] by applying an external radial electric field to the edge plasma by biasing or 'polarizing' an electrode and, thus, those experiments suggested that the radial electric field and induced poloidal rotation played a crucial role in the L–H transition. Since the increase in confinement in the spontaneous H mode was accompanied by a reduction in turbulence levels, as shown in DIII-D [3] and PBX-M [4], stabilization of turbulence by $\boldsymbol{E} \times \boldsymbol{B}$ shear, a general mechanism, was proposed [5] as the underlying cause for overall confinement, a hypothesis supported by early work at the TEXT [6] tokamak.

The velocity shear stabilization mechanism is now proposed to be responsible for a series of improved confinement regimes in tokamaks such as the H mode [7] and V–H mode [8] and recent experiments in TFTR have related the levels of local $\boldsymbol{E} \times \boldsymbol{B}$ shearing rates [9] to core transport barriers in reverse magnetic shear plasmas [10]. Polarization experiments in the TEXTOR tokamak [11, 12] have confirmed earlier CCT and TEXT results and significantly expanded the understanding of the role of the radial electric field and its bifurcation [13]. More recent experiments in TEXTOR-94 have shown the formation of a transport barrier in the plasma edge [14] as determined by the changes in density profiles during polarization [15] and have correlated those changes to the gradients of the radial electric field. A clear correlation between externally applied electric fields and a reduction in turbulence levels, without the gradient influence to cloud the issue, was first shown by our early work [16].

The existing theories of turbulence stabilization by $\boldsymbol{E} \times \boldsymbol{B}$ shear consider two main approaches, one is linear stabilization of modes [17, 18] and the other is decorrelation of turbulence [19, 20]. Both approaches predict a reduction in transport, although the nonlinear approach does not require total suppression of the underlying turbulence. In the linear approach, the effects of $\boldsymbol{E} \times \boldsymbol{B}$ shear are mode dependent

and therefore the details depend on the drive of the turbulence. Enhanced damping occurs by coupling unstable and stable modes [18]. In the non-linear approach, shear can affect non-linearly saturated turbulence and reduce transport by acting on both the amplitude and the cross-phase of the fluctuations. In general, the shearing rate γ_s must be comparable to $\Delta\omega_D$, the non-linear turbulence decorrelation rate in the absence of $\boldsymbol{E} \times \boldsymbol{B}$ shear. Additionally, it has been noted [21] in non-linear simulations that complete turbulence stabilization is achieved when the shearing rate γ_s is of the order of the linear growth rate γ_{ins} of the dominant mode in the plasma. However, the criterion is approximate and deviations by factors of 2 are not unusual. The shearing rate in an $\boldsymbol{E} \times \boldsymbol{B}$ driven velocity field is given by the radial derivative of the velocity, $V_{\boldsymbol{E}\times\boldsymbol{B}}$,

$$\gamma_{E\times B} = \left| \frac{dV_{E\times B}}{dr} \right| = \left| \frac{(RB_\theta)^2}{B} \frac{\partial}{\partial\psi} \frac{E_r}{RB_\theta} \right| \quad (1)$$

written in flux co-ordinates in terms of the major radius R, the poloidal magnetic field B_θ and the poloidal flux ψ [22].

In a tokamak, the radial electric field E_r, the radial pressure gradient $\nabla_r p_i$ and the toroidal v_ϕ and poloidal v_θ velocities are related by the radial force balance, given by the following equation:

$$E_r = \frac{1}{en_i} \nabla_r p_i - v_\theta B_\phi + v_\phi B_\theta. \quad (2)$$

The radial electric field can thus be created by a combination of a pressure gradient and a poloidal or toroidal velocity, which is the case in the spontaneous L–H transition [23], clouding the issue of causality and the roles of the various terms. The pressure gradient term, $(1/en_i)\nabla_r p$, which is all-important for the spontaneous L–H transition, is always negative in these experiments and negligible when compared with the positive $\boldsymbol{v} \times \boldsymbol{B}$ terms in Eq. (2).

In the work presented here, the thin ($\delta r = 1.5$ cm), rotating $\boldsymbol{E} \times \boldsymbol{B}$ shear layer induced by the electrode is characterized with high spatial resolution and correlated to the profiles of absolute and normalized turbulent quantities, including the turbulence driven radial particle flux. It is found that the amplitude of the fluctuations is reduced in the sheared layer and that fact, coupled to changes in the cross-phase, results in reduced turbulent transport and improved confinement. It is also found that low shearing rates are sufficient to affect the fluctuations. This work clearly establishes that the presence of velocity shear results in a reduction of turbulence induced radial particle flux, creating a transport barrier and an increase in particle confinement time. The polarization experiments greatly enhanced the ability to study the physics of turbulence stabilization in tokamaks by providing a high level of control and accessibility of diagnostics.

2. Experimental apparatus

These experiments were performed in ohmically heated (OH) plasmas with toroidal magnetic field $B_t = 2.25$ T, plasma current $I_p = 200$ kA and chord averaged density $\bar{n}_{e0} = 1.0 \times 10^{13}$ cm^{-3}. The discharge was tailored to reduce the heat flux to the electrode. The electrode is mushroom shaped and built of graphite composites 1.5 cm in thickness and 10 cm in diameter, and is introduced to a radius of 41 cm as described in previous work [7]. The ALT-II toroidal belt limiter [24] is nominally located at 46 cm, but in these experiments the plasma was shifted down (1 cm) and out (1 cm) to assure that ALT-II is the only limiter, resulting in a slightly reduced (45.5 cm) plasma radius.

The data were obtained using two fast reciprocating probe arrays [25] featuring five tips. The main reciprocating probe is located at the outer midplane of the tokamak and the second probe is located at the top. TEXTOR edge plasmas are toroidally symmetric due to the ALT-II belt limiter. The data for the turbulent measurements are digitized at 1 MHz with a 10 bit digitizer and filtered by low pass 500 kHz anti-aliasing filters. We find that the power spectrum decays very quickly with frequency and is significant only up to 250 kHz, thus a bandwidth of at least 500 kHz is desirable for turbulence measurements.

The voltage is applied to the electrode as a 100 ms linear ramp starting at 0.9 s and then held constant for 1.5 s, as shown in Fig. 1(e). The electrode current increases linearly until the radial electric field bifurcation occurs at 1.1 s, resulting in a core density increase by a factor of 1.5 (Fig. 1(d)) and a reduction in the electrode current (Fig. 1(e)). The discharge then progresses to a quasi-stationary state as shown in Figs 1(c) and (d). The probe enters the plasma at $t = 1.6$ s (Fig. 1(a)), sampling the shear layer, as shown by the increase in floating potential (Fig. 1(b)). The radial electric field increases with voltage and eventually bifurcates from a broad profile to a narrow one in the region between $r = 43.2$ and $r = 44.8$ cm (Fig. 2), reaching a maximum value of ~500 V/cm, as discussed in detail in our previous work [16, 13]. The radial electric field maximum is

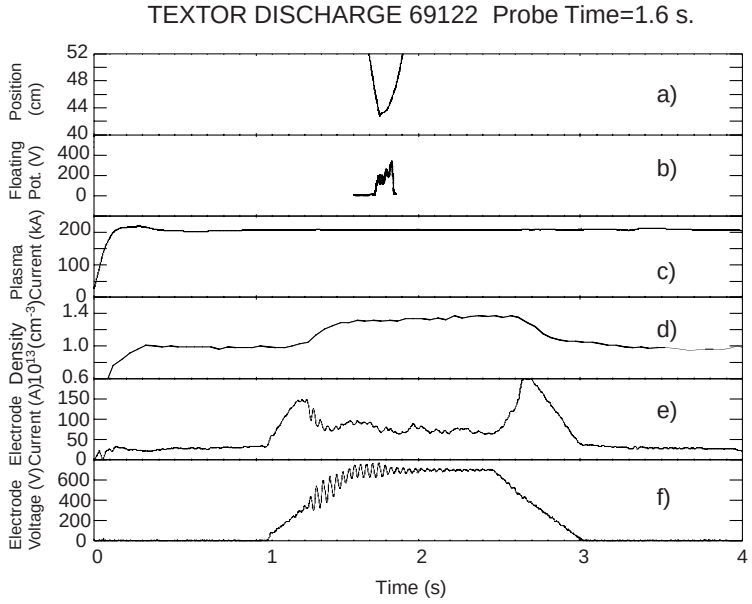

Figure 1. Time traces of a typical TEXTOR polarization discharge showing the (a) probe position, (b) floating potential measured by the probe, (c) plasma current, (d) plasma density, (e) electrode current and (f) electrode voltage. The voltage is applied at about 1.0 s and the transition occurs at 1.1 s.

marked by a dashed line consistently in all the radial profiles. Upon bifurcation, the radial conductivity increases suddenly in a narrow region [13] which, in the framework of neoclassical theory, is determined by a delicate balance between viscosity and ion–neutral friction, both featuring a strong radial variation in front of the limiter. The radial electric field bifurcation has a well defined and reproducible (within 20%) threshold at an electrode voltage V_{el} of ∼450 V and an electrode current I_{el} of ∼170 A, as seen in Figs 1(e) and (f) and Fig. 11. The hill associated with the radial electric field is of the order of 1–1.5 cm wide, which is 10–20 times the ion or electron gyroradius (0.8–1 mm) and of the order of the poloidal Larmor gyroradius for TEXTOR.

The plasma conditions are labelled consistently throughout the article. The condition of high particle confinement and shear after the bifurcation is labelled 'H mode' and the background, unpolarized, low confinement condition, 'L mode'. The condition where the electrode is energized and the plasma is exposed to some shear is labelled 'L–H' if progressing towards bifurcation and 'H–L' if leaving it. The bifurcation of the electric field and its timing are identified by the sudden decrease of the polarization electrode current and the H_α signal.

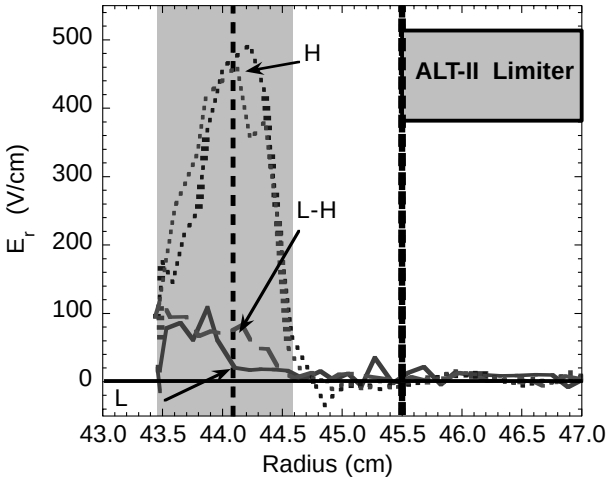

Figure 2. Radial electric field measured by the probe for L, L–H and H mode conditions. The peak of the electric field and the shear layer are marked by a dashed line and a shaded box, respectively.

3. General description of polarized edge plasma

As the electrode is polarized, the edge density steepens considerably in the region between the

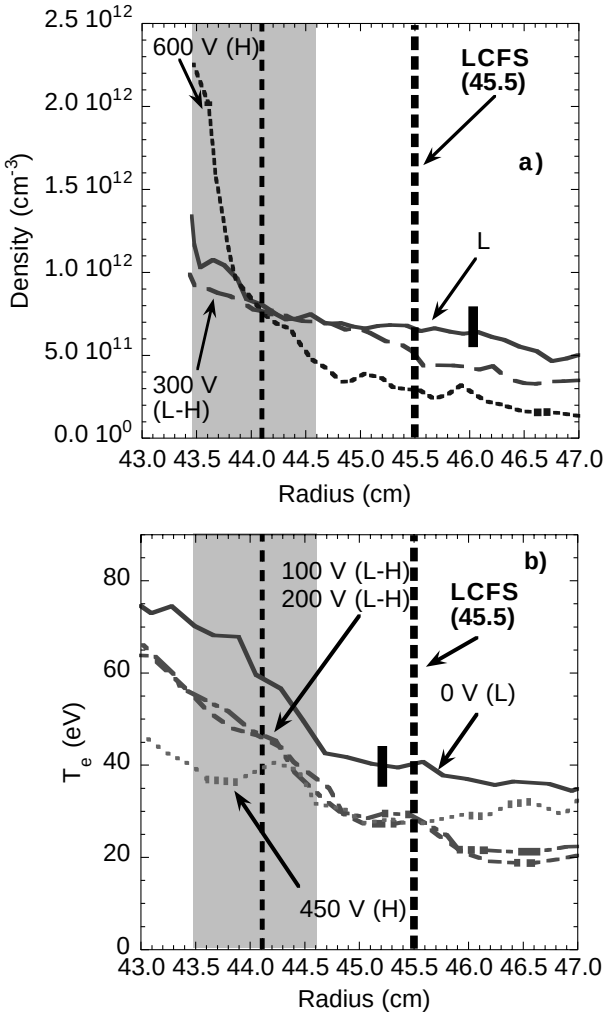

Figure 3. Profiles of (a) electron density and (b) electron temperature for L mode, H mode and low shear discharges (L–H). The shear layer is shown by a shaded box and the location of the radial electric field maximum is marked by the double dashed line.

electrode (at 41.5 cm) and the limiter (at 45.5 cm) and the temperature profile flattens, as shown in Fig. 3(b), reflecting increased radiation losses. The steepening of the density profile (Fig. 3(a)) indicates the formation of a transport barrier in the narrow (1.5 cm) region where E_r and the velocity shear are large (Fig. 2). The shear layer is consistently shown as a shadowed box in all figures. The temperature inside the barrier is reduced by 40–50%, resulting in a considerably flattened profile. The combined changes of the T_e and n_e profiles result in a mostly unchanged electron pressure profile up to 45 cm, in contrast with the marked increase in electron pressure characteristic of a spontaneous H mode.

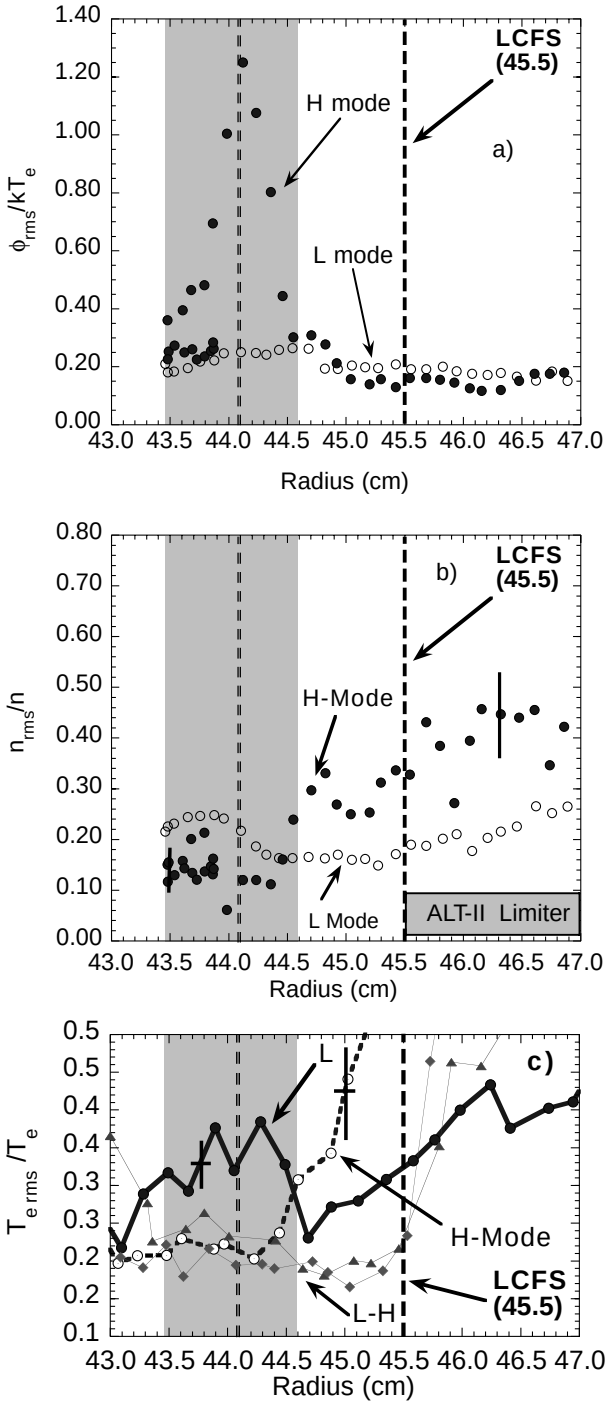

Figure 4. Normalized turbulence levels of (a) potential, (b) density and (c) temperature. The maximum of the radial electric field is marked with a vertical dashed line.

The normalized density and temperature fluctuation levels are reduced by 40–50% at the shear layer, whereas the potential fluctuation levels increase by a factor of ∼6, as shown in Fig. 4, partly due to the decrease in temperature and partly to the presence of coherent modes. The fluctuation ordering in the

L mode edge is $\tilde{T}_e/T_e \approx 0.35 > \tilde{\phi}/kT_e \approx \tilde{n}/n \approx 0.25$ for these low density OH plasmas. The changes in the plasma potential and temperature fluctuations are fairly symmetric about the peak of the electric field (marked by a dashed line), but the changes in the density fluctuations and cross-phase are asymmetric and dependent on the sign of ∇E_r, a result that will be discussed later.

4. Turbulent particle flux

The turbulent particle flux, $\tilde{\Gamma}_r$, depends on the RMS values of the density $\langle\tilde{n}_e^2\rangle^{1/2}$ and poloidal electric field $\langle\tilde{E}_\theta^2\rangle^{1/2}$, their coherence $\gamma_{\tilde{E}\tilde{n}}$ and α, the $\tilde{n}_e$–$\tilde{E}_\theta$ cross-phase, as [26]

$$\tilde{\Gamma}_r = \frac{\langle\tilde{E}_\theta\tilde{n}_r\rangle}{B_\phi} = \frac{\langle\tilde{n}_e^2\rangle^{1/2}\langle\tilde{E}_\theta^2\rangle^{1/2}}{B_\phi}\frac{\langle\tilde{E}_\theta\tilde{n}_r\rangle}{\langle\tilde{n}_e^2\rangle^{1/2}\langle\tilde{E}_\theta^2\rangle^{1/2}}$$
$$= \frac{\langle\tilde{n}_e^2\rangle^{1/2}\langle\tilde{E}_\theta^2\rangle^{1/2}}{B_\phi}\gamma_{En}\cos\alpha \qquad (3)$$

where the brackets denote ensemble averaging. We emphasize that the *absolute* RMS levels of the density and poloidal field are the relevant fluctuating quantities that affect the radial turbulent particle flux, as seen in Eq. (3), and not the normalized levels. The density potential cross-power spectrum is the relevant quantity for frequency space calculations. Therefore, we have concentrated our discussion on the aforementioned quantities.

The fluctuation driven particle flux shown in Fig. 5(d) decreases from 6×10^{15} to 0.2×10^{15} cm^2 s^{-1}, zero for practical purposes, at the LCFS. The particle flux is essentially quenched in the region $r = 43.5$–50 cm and even becomes negative at $r \sim 43.8$ cm, which is not the region where the electric field reaches a maximum but where its derivative ∇E_r is positive. The reduction in radial particle flux across the shear layer can be traced to changes in $\tilde{E}_\theta$ (Fig. 5(a)), $\tilde{n}$ (Fig. 5(b)) and especially their cross-phase (the coherence is reduced from 0.6 to 0.35), $\cos\alpha$ (Fig. 5(c)), and expected as some of the effects of velocity shear stabilization [27].

The changes in $\tilde{E}_\theta$, $\tilde{n}$ and $\tilde{\Gamma}_r$, although initiated in the shear layer (notice the L–H traces in Fig. 5), eventually extend across the entire SOL, as seen in spontaneous H modes [28]. The non-localization of the turbulent flux reduction could be connected to either a reduction of the driving sources of the turbulence by the changes in the profiles and their gradients or to the stabilization of a radially extended (i.e. long radial correlation length) turbulence source.

The particle flux can be calculated alternatively in frequency space in terms of the density and potential fluctuation cross-power spectra $P_{n\phi}(\omega)$, the poloidal wavenumber $k_\theta(\omega)$ and the phase between the density and potential fluctuations $\alpha_{n\phi}(\omega)$ as [29]

$$\Gamma(\omega) = \frac{2}{B}\int \big|P_{n\phi}(\omega)\big| k_\theta(\omega)\sin\alpha_{n\phi}(\omega)d\omega. \qquad (4)$$

The probe data can be analysed in frequency space in the framework of Eq. (4) and the results are displayed in Fig. 6. The data between the radii $r = 43.5$ cm and $r = 44.5$ cm have been used in order to provide good statistics, with the consequence that the frequency resolved quantities are averaged over ~0.5–0.7 cm, losing radial resolution. An important observation is that the coherence between density and potential decreases from a robust 0.6 across the spectrum (0–500 kHz) in L mode to 0.2–0.4 in H mode, while the cross-power spectrum becomes flat and broad and is reduced by a factor of 5–10. This reduction partially explains the suppression of radial particle flux as discussed previously. A significant fraction of the power remains at very low frequencies (quasi DC) in H mode and coherent modes are sometimes seen at $f \sim 40$ kHz and $f \sim 70$ kHz, bearing nearly half the radial particle flux. The k_θ spectrum is linear and its average value is reduced from 2–3 cm^{-1} in L mode to 1 cm^{-1} in H mode, partly due to the large phase velocity of the turbulence in the layer. The shift in k_θ is partially responsible for the reductions in $\tilde{\Gamma}_r$ and $\tilde{E}_\theta$. The phase between density and potential remains at 1.7 rad ($\approx \pi/2$) across the spectrum. An important result from these data is that the density and potential fluctuations become decorrelated during H mode, as shown by the low coherence, resulting in a significantly reduced cross-power spectrum.

5. Turbulent heat flux

Cross-field heat transport can be expressed [30], omitting species indexes (e and i), as the sum of convective and conductive, classical (c) and anomalous ($\sim$) terms,

$$Q_{tot} = \bar{q}_c + \frac{3}{2}\bar{T}\bar{\Gamma}_{rc} + \tilde{Q}_{cond} + \tilde{Q}_{conv}$$
$$= \bar{q}_c + \frac{3}{2}\bar{T}\bar{\Gamma}_{rc} + \frac{3}{2}\bar{n}\frac{\langle\tilde{T}\tilde{E}_\theta\rangle}{B_\phi} + \frac{3}{2}\tilde{\Gamma}_r\bar{T} \qquad (5)$$

where $\bar{n}$ and $\bar{T}$ are the average density and temperature and Γ_r is the radial particle flux. The overbar denotes averaged quantities and the brackets denote

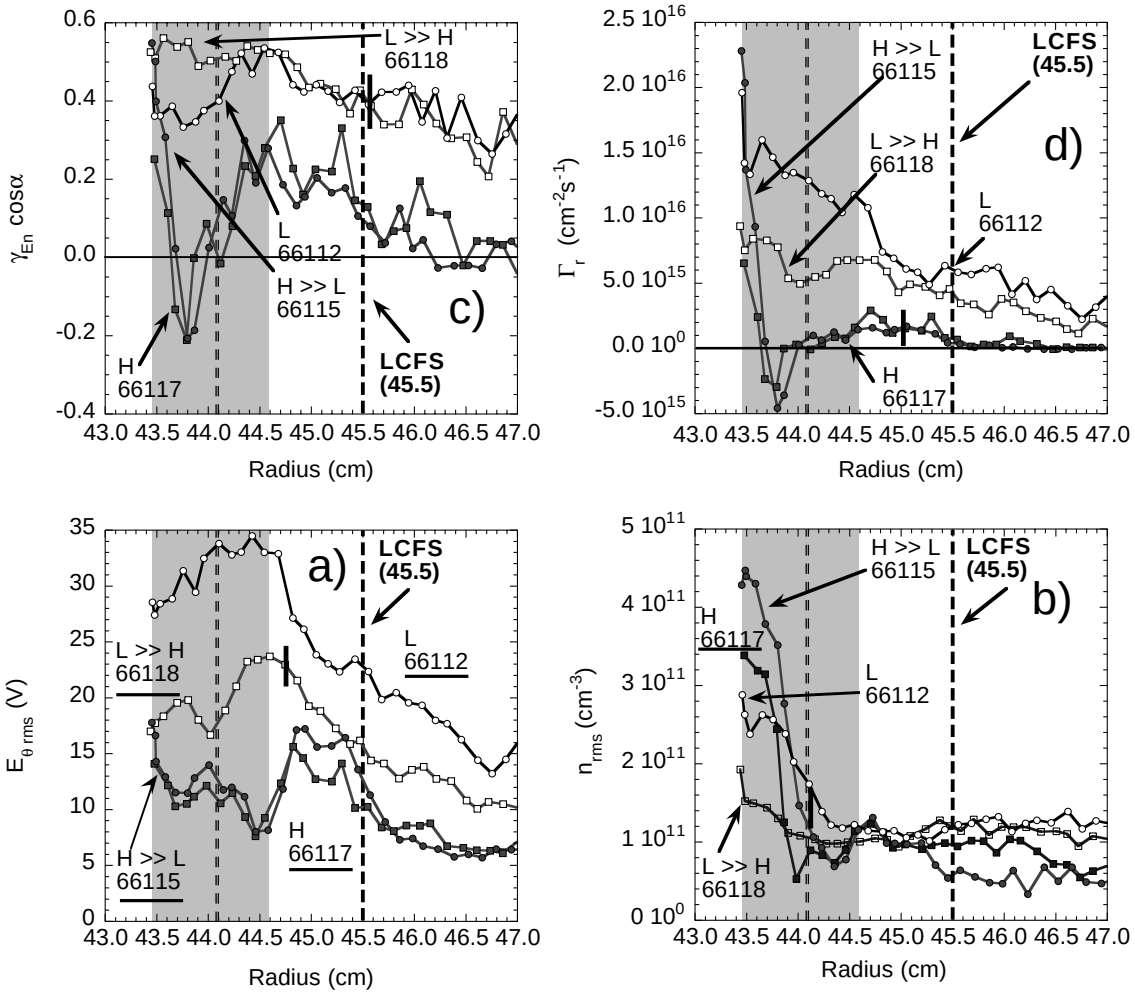

Figure 5. Radial profiles of (a) $\tilde{E}_\theta$, (b) $\tilde{n}$, (c) $\cos\alpha$ and (d) radial turbulent flux. The L $\gg$ H values are somewhat in between the steady state ones, showing partial stabilization before bifurcation and a strong effect confined to the shear layer.

ensemble averaging. The anomalous conducted heat flux can be written in terms of the temperature fluctuations $\tilde{T}_e$, poloidal field fluctuations $\tilde{E}_\theta$ and their cross-phase angle α^{ET} as

$$\begin{aligned}\tilde{Q}_{cond} &= \frac{3}{2}\bar{n}\frac{\langle\tilde{T}\tilde{E}_\theta\rangle}{B_\phi} \\ &= \frac{3}{2}\bar{n}\frac{\langle\tilde{T}^2\rangle^{1/2}\langle\tilde{E}_\theta^2\rangle^{1/2}}{B_\phi}\frac{\langle\tilde{E}_\theta\tilde{T}\rangle}{\langle\tilde{T}^2\rangle^{1/2}\langle\tilde{E}_\theta^2\rangle^{1/2}} \\ &= \frac{3}{2}\bar{n}\frac{\langle\tilde{T}^2\rangle^{1/2}\langle\tilde{E}_\theta^2\rangle^{1/2}}{B_\phi}\gamma_{ET}\cos\alpha^{ET}. \qquad (6)\end{aligned}$$

The turbulent particle flux, $\tilde{\Gamma}_r$, was defined in Eq. (3).

An important result of this work [31] is that temperature fluctuations are found to be reduced by a factor of 1.5–2 in the weaker shear conditions (100, 200, 400 V) and by a factor of 2 after the bifurcation to H mode (450 V) as shown in Fig. 7. Normalized temperature fluctuations (Fig. 4(c)), which are similar for weak and strong shear conditions, are reduced by a factor of ∼2. The experimental results can be understood by considering a simple model for the response of electron temperature fluctuations to the potential. The temperature fluctuation, $\tilde{T}$, under advection of the mean temperature gradient by the $\boldsymbol{E}\times\boldsymbol{B}$ velocity, is governed by

$$\begin{aligned}&(\partial/\partial t + V_0 r^{-1}\partial/\partial\theta + B^{-1}\nabla\phi\times\boldsymbol{b}\cdot\boldsymbol{\nabla} - \chi_\parallel\nabla_\parallel^2)\tilde{T} \\ &\quad = B^{-1}r^{-1}(\partial\phi/\partial\theta)d\bar{T}/dr \qquad (7)\end{aligned}$$

where $\chi_\parallel$ is the parallel thermal conductivity, V_0 is the poloidal $\boldsymbol{E}\times\boldsymbol{B}$ shear flow, ϕ is the fluctuating electrostatic potential and $\boldsymbol{b}$ is the unit vector in the

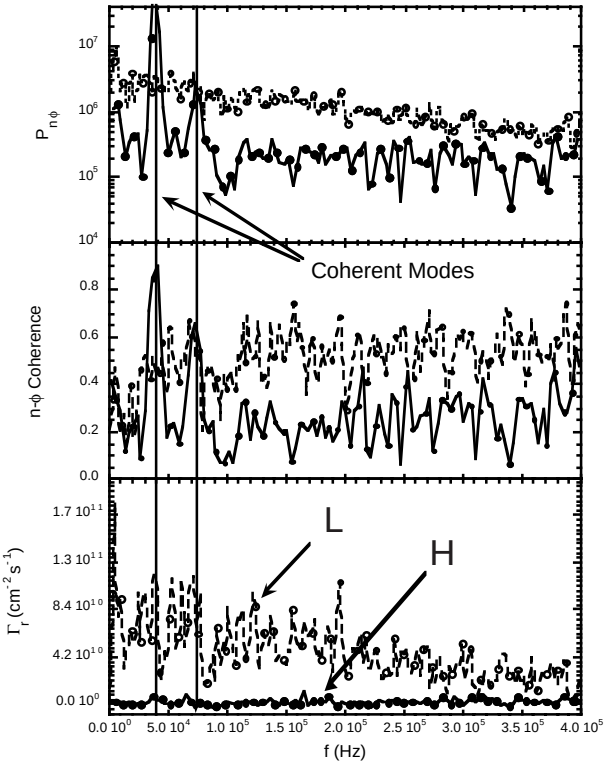

Figure 6. Cross-power spectrum (top), coherence (middle) and radial particle flux (bottom) shown versus frequency for frequencies of up to 400 kHz. High (H) and low (L) confinement discharges are compared. The location and existence of coherent modes are highlighted.

direction of the magnetic field. If $\tilde{T}$ is governed by a collective excitation whose linear growth rate is ω_{ins} and whose radial mode width is W, the linear temperature response becomes:

$$\tilde{T} = \frac{B^{-1}\dfrac{\partial\phi}{r\partial\theta}\dfrac{d\bar{T}}{dr}}{(\omega_{ins} + iV_0Wm/r - \chi_\parallel W^2m^2/R^2q^2L_q^2 + \Delta\omega_D)} \quad (8)$$

where m is the poloidal mode number, $L_q^{-1} = q^{-1}dq/dr$ is the scale length of the safety factor q and R is the major radius. The second to fourth terms of the denominator are the $\boldsymbol{E}\times\boldsymbol{B}$ shearing rate, the rate of parallel thermal conduction and the non-linear decorrelation rate, respectively. In a situation where the parallel thermal conductivity term is significantly larger than the growth rate, non-linear decorrelation rate or maximum value of the flow shear term, increases of flow shear lead to little change in temperature fluctuations because parallel thermal conduction dominates the response. On the other hand, suppression of $\tilde{T}$ should be observed

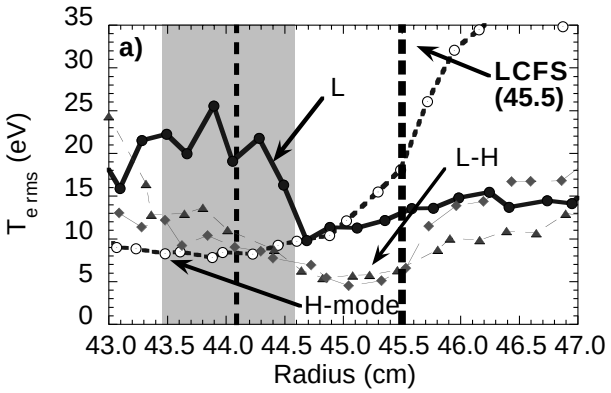

Figure 7. Radial profile of temperature fluctuations. The apparent increase in the SOL during H mode is a diagnostic artefact due to reduced T_e and resulting loss of signal to noise ratio.

if the shearing rate becomes larger than any of the other rates in the response. The terms in Eq. (7) can be estimated by considering resistive pressure gradient driven turbulence, which is an appropriate edge model for these plasmas and has been studied extensively in the context of shear induced transport reduction. The growth rate and mode width are given by

$$\omega_{ins} = [\kappa(m/r)L_s\eta^{1/2}P_0'\rho_m^{-1/2}B^{-1}]^{2/3}$$

and

$$W = [L_s^4\rho_m\eta^2\kappa P_0'(m/r)^{-2}B^{-4}]^{1/6}$$

where κ is the magnetic field curvature, $L_s = RqL_qr^{-1}$ is the magnetic shear scale length, η is the resistivity, P_0' is the mean pressure gradient and ρ_m is the mass density. For the edge of the TEXTOR tokamak, the poloidal wavenumber m/r is 1–2 cm^{-1}, R = 2.2 m, T_0 = 50 eV, $n = 2.5\times10^{12}$ cm^{-3}, B = 1.8 T, $P_0'/nT = 1$ cm^{-1} and $L_s \cong 2R = 4.4$ m. For $m/r = 1$ cm^{-1}, the growth rate is 10^5 s^{-1} and the parallel thermal conduction is 5×10^4 s^{-1}. From measurements, $\Delta\omega_D = 5\times10^5$ s^{-1}. All of these are less than $\omega_{\boldsymbol{E}\times\boldsymbol{B}} = V_0'Wm/r = 10^6$ s^{-1}, indicating that temperature fluctuations should be reduced, as observed.

The anomalous conducted electron heat profile, and its change with shear, can be calculated from Eq. (6) by using the measured values of $\tilde{T}_e$, $\tilde{E}_\theta$ and $\bar{n}_e$ and assuming a strong $\tilde{T}_e$–$\tilde{E}_\theta$ correlation (i.e. $\gamma_{\tilde{E}\tilde{T}}\cos\alpha^{ET} = 1$). The calculated heat flux, shown in Fig. 8(a), is an upper limit for sheared plasmas (H) and accurate for the L conditions since a strong $\tilde{T}_e$–$\tilde{E}_\theta$ correlation has been documented for non-sheared

plasmas in a variety of tokamaks [32, 33]; therefore, the value of $\gamma_{\tilde{E}\tilde{T}} \cos\alpha^{ET}$ in H mode could only be reduced further by velocity shear effects. Even this upper limit shows a factor of 4 reduction in the conducted heat flux for strong $\boldsymbol{E} \times \boldsymbol{B}$ shear, (Fig. 8(a)), a result from reductions in $\tilde{T}_e$ (Fig. 7) by a factor of 2–3 and in $\tilde{E}_\theta$ by a factor of 3 across the shear layer. The anomalous convected electron heat flux (Fig. 8(b)) also decreases in the shear layer as a result (Eqs (3) and (5)) of reductions in $\tilde{E}_\theta$ (Fig. 5(a)) by a factor of 3 and in $\gamma_{\tilde{E}\tilde{n}} \cos\alpha$, which becomes negative at 43.7 cm (Fig. 5(c)), and causes a change in flux direction. The conduction term is larger than the convection term by a factor of 7–10 in L mode conditions and, if quenched, should become an energy barrier generator.

The power balance for these discharges is summarized in Table 1. The difference between the input and radiated powers P_{in} and P_{rad} (7%) is convected and conducted across the LCFS. The total power $\tilde{P}^e_T$ carried across the LCFS by the sum of turbulent electron convection $\tilde{P}^e_{conv}$ and conduction $\tilde{P}^e_{cond}$, if assumed uniform over the cross-section, can account for ∼60 and ∼18% of the total in L and H mode plasmas, respectively. If an equal ion contribution is assumed and added [32], then $\tilde{P}^{i+e}_T \sim 120\%$ (OH) and ∼36% (H mode) of the total power. Therefore, anomalous heat transport accounts for the power balance in L mode, but not in H mode, conditions. Insight is obtained by considering the power convected by the total particle flux inferred from H_α, $P^{H_\alpha}_{conv}$, which compares well with $\tilde{P}^{e+i}_{conv}$ in L mode conditions but is much higher in H mode conditions. Once the dominating turbulent particle flux is quenched, other sources of transport that are significant (∼40%), but unknown, become apparent and are in agreement with the discussion in Section 10. If transport reductions were limited solely to the particle flux in TEXTOR (i.e. no reduction in conducted heat flux) the total heat flux would experience only a slight decrease from 194 to 160 kW and mimic the results where a particle barrier, and not an energy barrier, was observed [34].

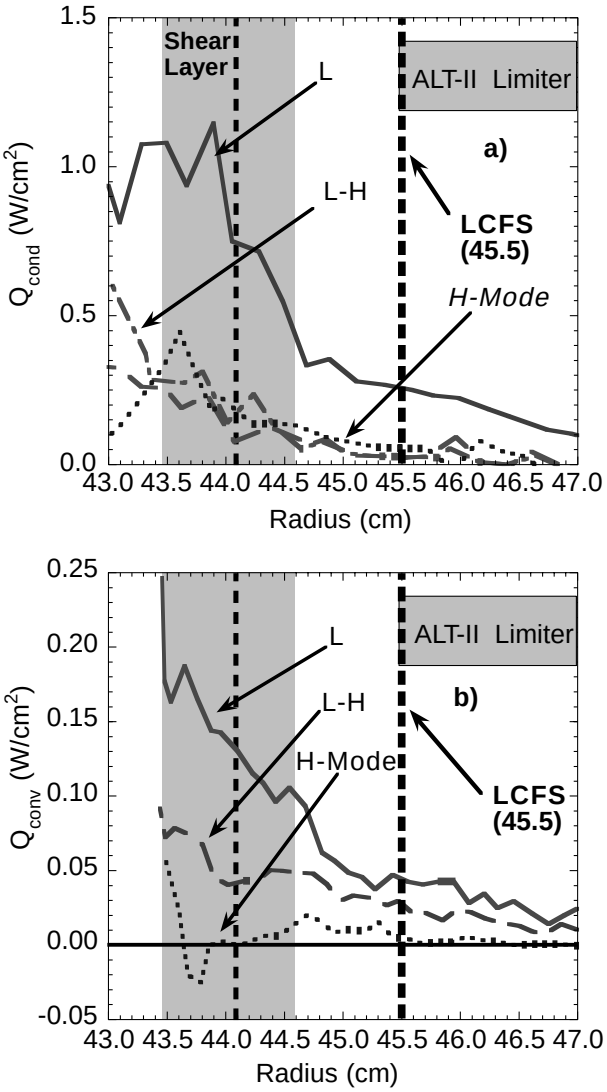

Figure 8. Radial profiles of (a) the conducted and (b) the convected radial heat flux. The conducted heat is 4–10 higher than the convected heat.

6. Poloidal velocity and shearing rate

To establish a unequivocal correlation between the reduction of turbulence and the mechanism of

Table 1. Power balance for the discharges considered (All powers are in kilowatts)

Mode	P_{in}	P_{rad}	$P_{in} - P_{rad}$	$P^{H_\alpha}_{conv}$	$\tilde{P}^e_{conv}$	$\tilde{P}^e_{cond}$	$\tilde{P}^e_T$	$\tilde{P}^{i+e}_T$
L	250	87	163	41	17	80	97	194
H	281	187	94	23	0.22	16	16.22	32.5

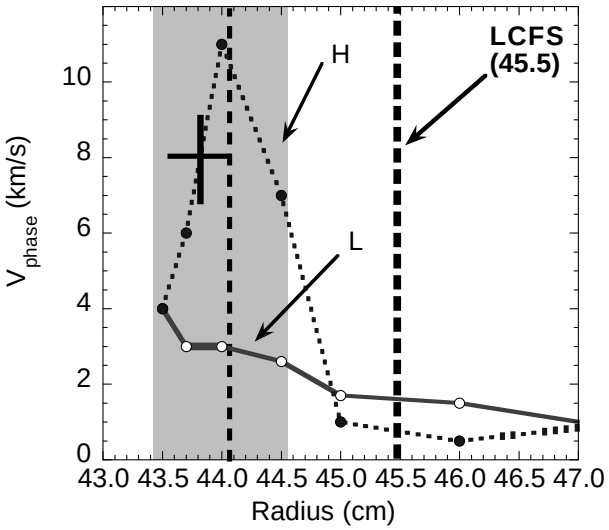

Figure 9. Measured phase velocity for bifurcated polarized discharges (filled symbols) and background (L) discharges. The turbulence propagates in the ion diamagnetic drift direction. The uncertainty in radius for the phase velocity is ∼0.5 cm and stems from the need to average over a time long enough to provide good statistics.

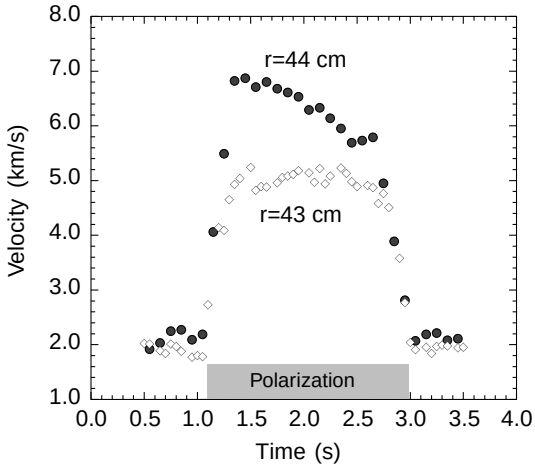

Figure 10. Poloidal velocity from Doppler shift of the CII line. A rotation, up to 7 km/s, is apparent as soon as the electric field bifurcates at 1.15 s. The radii shown denote the diagnostic chords only. The radial resolution of the diagnostic is lower than the width of the shear layer; thus the equivalent of spatial averaging is performed.

velocity shear stabilization, clear and precise measurements of the sheared velocity profile and the turbulence profiles are required. The velocity of the poloidally rotating layer can be measured directly from the phase velocity of the turbulence and impurity spectroscopy, and is correlated to that inferred from experimental measurements of the radial electric field. The phase velocity of the turbulence can be calculated from the following (basically linear) dispersion relation:

$$v_{ph} = \frac{\omega}{k} \approx \frac{\Delta\omega}{\Delta k} = \frac{2\pi\Delta f}{\Delta k}. \qquad (9)$$

This is deduced from the conditional probability spectrum $s(k|\omega)$ as defined by Beall et al. [35] and obtained with a two point technique in the region of large radial electric field and averaged over ∼0.5 cm to improve the statistics. We obtain a profile of poloidal velocity, shown in Fig. 9, which peaks at a speed of ∼12 km/s and compares favourably (due to profile averaging effects) with the value of 19 km/s calculated from the peak value of the measured radial electric field. Poloidal rotation measurements made using the Doppler shift of the CII line at the plasma with ∼2 cm resolution, possibly resulting in underestimated velocity values, indicate poloidal rotation in the $\boldsymbol{E}\times\boldsymbol{B}$ direction at ∼7 km/s, as shown in Fig. 10. The measured poloidal rotation velocity corresponds to Mach 0.3 for the conditions in this discharge (deuterium, if $T_i = T_e = 30$–40 eV).

The shearing rate γ_s calculated with Eq. (1) by using the experimental poloidal velocity profile was compared with the non-linear decorrelation rate of the turbulence $\Delta\omega_D$ inferred from the autocorrelation function [6] $R(\tau, r) \equiv \langle z(t, r)z(t + \tau, r)\rangle$ of the fluctuating ion saturation current in a region where the $\boldsymbol{E}\times\boldsymbol{B}$ shear is near zero. We find that $\gamma_s \sim 1\times10^2$ s^{-1} $\approx \Delta\omega_D = 9\times10^5$ s^{-1}; therefore the shearing rate imposed on the plasma edge is of the order of that needed to stabilize the turbulence in TEXTOR.

Our calculations then localized the shear layer with 2 mm accuracy and established by three different methods that the shearing rate is high and of the order of 1×10^6. Furthermore, correlation of the shear layer with the profiles of turbulent quantities has established that the turbulence is initially modified most strongly at the location of the layer although the effects are later spread to the entire SOL, probably by non-linear effects.

7. Curvature and low shear effects

High resolution profile measurements were taken in plasma conditions before the electric field bifurcation, at the bifurcation and during well-defined

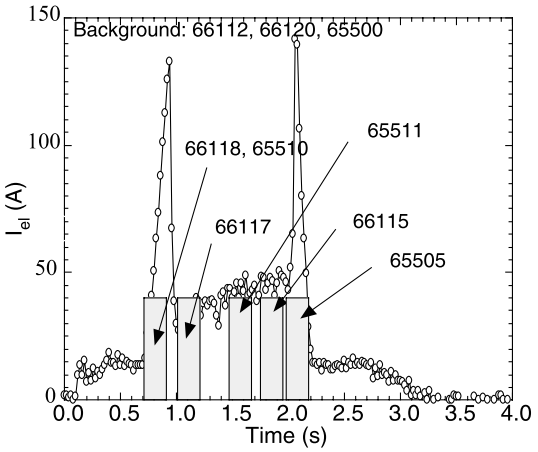

Figure 11. Times at which the fast probe was inserted in the plasma superimposed on a plot of electrode current against time. The five digit numbers refer to particular TEXTOR plasma discharges.

H modes by varying the probe insertion time to different times during the discharge, as shown in Fig. 11. Two distinct radial profiles for each quantity, separated by ∼80 ms, are obtained for each probe insertion corresponding to the inward and outward strokes. The profiles of plasma parameters and turbulent quantities for a family of polarized discharges are shown in Figs 2, 3, 4, 5 and 7. The following features are notable in those profiles:

(a) *Modest shear. Before electric field bifurcation:* When a voltage is applied to the electrode but no transition has yet occurred (the L–H case), the radial electric field features a broad profile peaking at ∼100 V/cm and therefore a modest shear is present, as discussed in detail in previous work [16]. The data is in a region where $\nabla E_r < 0$ or ∼0. The data show no strong features in the shear layer:

- A reduction of ∼30% in $\tilde{E}_\theta$ levels is seen (Fig. 5(a)) across the shear layer and the whole SOL.
- A reduction of ∼40% in $\tilde{n}$ levels is observed (Fig. 5(b)) in the shear layer, no change in the SOL.
- A slight increase in $\gamma_{En}\cos\alpha$ occurs in the shear layer (Fig. 5(c)), no change in the SOL.
- The combination of the variations above result in a reduction of $\tilde{\Gamma}_r$ by a factor of ∼2 (Fig. 5(d)) over the shear layer and a very slight reduction in the SOL.

(b) *High shear. After electric field bifurcation:* During this phase, the electric field has reached values of 500 V/cm and its peak is located at ∼44.1 cm. Zones where $\nabla E_r > 0$ or $\nabla E_r < 0$ can be easily identified, the errors on the second derivative of E_r are too large to draw conclusions and we will strongly qualify the hints in the data. The data become clearly asymmetric on the shear layer, featuring:

- A reduction by a factor of 3 occurs in $\tilde{E}_\theta$ levels across the shear layer and SOL.
- An increase in $\tilde{n}$ levels over those of L mode occurs where $\nabla E_r > 0$ and possibly $E_r'' > 0$, but a significant reduction occurs where $\nabla E_r > 0$ and possibly $E_r'' < 0$, while a mild reduction occurs where $\nabla E_r < 0$ and possibly $E_r'' < 0$. No change is seen in the SOL.
- The cross-phase $\gamma_{En}\cos\alpha$ is affected across the shear layer and the SOL and becomes negative in the region $\nabla E_r > 0$ and $E_r'' \approx 0$, resulting in inward particle flux over a narrow region at $r \sim 43.8$ cm. (Fig. 5(c)).
- The combination of the variations above results in an overall suppression over the shear layer and the SOL. Most importantly, the flux is reversed at $r = 43.8$ cm.

It can be concluded that low shearing rates are sufficient to significantly affect, and reduce, the fluctuations and the particle flux in the shear layer and that a transport barrier precedes the electric field bifurcation, in agreement with observations [15] that the density and total number of particles start to rise well before the L–H transition. The $\tilde{n}_e$–$\tilde{E}_\theta$ cross-phase plays a crucial role in reducing turbulent radial particle fluxes, verifying the motivation behind some theoretical models [27]. Most importantly, the sensitivity of $\tilde{n}/n$, $\tilde{n}$ and the cross-phase, particularly the sign change of the cross-phase, to the sign of ∇E_r provides solid evidence in support of theoretical work including shear and its derivatives as a phase altering [27] mechanism. Note that the change in $\cos\alpha$ is dependent on the sign of V_0 instead of the predicted [36] $V_0'^2$ for resistive pressure gradient driven turbulence in low shear conditions.

The above results can be discussed in the framework of the existing theoretical and numerical simulation background. Initial theoretical work focused on the effects of the sheared flow on the fluctuation levels only [5], but more recent numerical simulations [37] on resistive pressure gradient turbulence (RPGDT) demonstrated reduced transport due to modification of the cross-phase by shear and, most importantly, curvature in the poloidal $\boldsymbol{E} \times \boldsymbol{B}$ flow.

Further work [27], also on RPGDT, demonstrated analytically that both flow shear and curvature can affect the cross-phase as well as the fluctuation levels, but the effect was independent of the sign of the first or second derivative and only valid for weak shear conditions. Furthermore, other work [38–40] has demonstrated that the sign of the curvature of the $\boldsymbol{E} \times \boldsymbol{B}$ velocity is relevant under certain conditions. It is to be noticed that much of the existing work is mode specific and valid only in the weak shear limit, therefore, no general result is available.

8. Particle and energy confinement

The reduced turbulence induced radial particle transport and turbulence occurs concomitantly with a large (x1.5) density increase and a reduction in recycling, suggesting increased particle confinement. Quantitative measurements of H_α are used to calculate the particle confinement time τ_p and its temporal variation by:

(a) Including poloidal and toroidal variations of recycling using 2-D images obtained by an absolutely calibrated CCD camera.
(b) Measuring the recycling at the polarizing electrode.

We first examine the influence of the electrode on the recycling by comparing otherwise identical discharges (69111 or 65497, 69113 and 65498) with and without the electrode inserted. The H_α signal at five different locations is unchanged within an 8% sensitivity level, indicating that the electrode is not acting as a significant source of recycling. Furthermore, the H_α emission at the electrode, monitored using a CCD camera, increases 100% during the electrode current ramp-up while all other H_α signals remain unperturbed, indicating that the electrode holds less than 4% of the recycling. Once the transition occurs, the H_α signal from the electrode decreases by about 50%, as seen in Fig. 12.

The H_α emission in TEXTOR during polarization has been analysed with a calibrated CCD camera [41] observing the ALT-II limiter. The camera signal is integrated over a large area, including an entire limiter blade and parts of the wall, to increase the signal to noise ratio and to account for the contribution of extended poloidal 'halos', which have been shown to contain about 50% of the signal in low plasma density discharges such as these. We infer τ_p increases of 100%, from 35–40 ms in the L mode to 80–90 ms in H mode, as shown in Fig. 13. Note that τ_p already

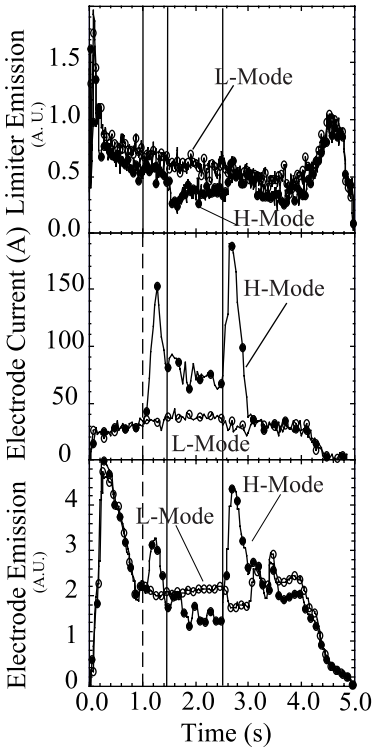

Figure 12. Evolution of signals from the H_α emission from the limiter (top) and the polarization electrode (bottom) and comparison with the electrode current (middle). The traces corresponding to the discharge with no voltage are labelled with open symbols and those corresponding to the polarized discharge are labelled with filled symbols.

increases by 50% before the bifurcation, but the extra recycling taken by the electrode is bound by 8%. We conclude that τ_p is already increasing before the transition occurs, consistently with the observed precursor reduction of radial turbulent flux.

It has been shown [11] that τ_E increases (by 30%) in these experiments after the bifurcation of the electric field. We have evaluated τ_E by integrating the pressure profiles (assuming $T_i = T_e$) and including the contribution from the density time dependence as

$$\tau_E = \frac{E}{P_{in} - \dfrac{dE}{dt}}. \tag{10}$$

The polarization power is reduced to 21–35 kW after the transition due to the low electrode current (30–50 A at 700 V) and therefore contributes only 10–15% to the total power (about 260 kW). We expect most of this power to be deposited, and also dissipated, in the edge and SOL without

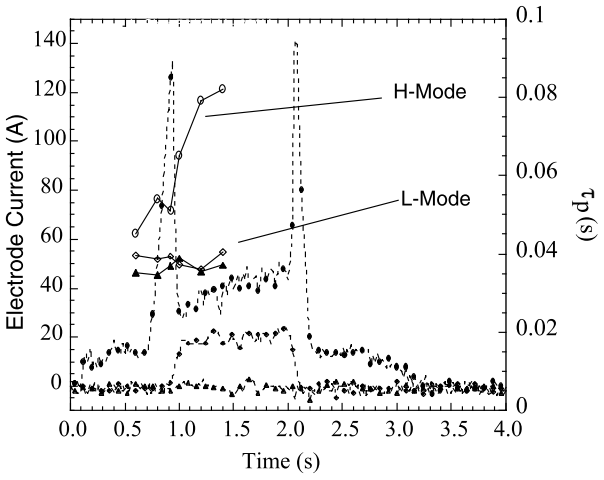

Figure 13. Traces of the electrode current I_{el} versus time for $V_{el} = 0$, 300 and 700 V are superimposed on measurements of τ_p (error bars of 25%) from H_α. In the bifurcated discharge, τ_p increases before the bifurcation of the electric field at 0.9 s.

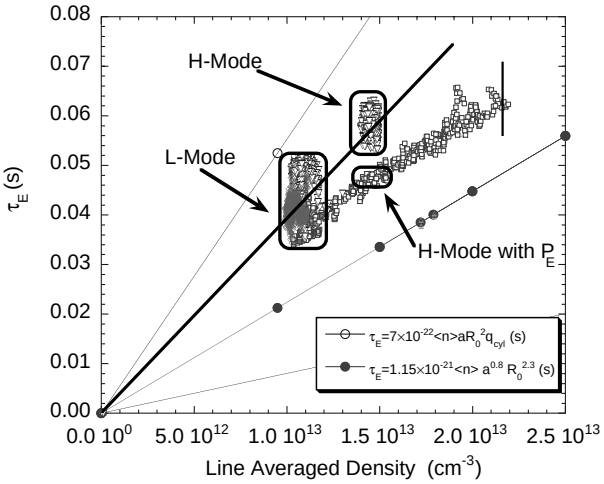

Figure 14. Measurements of τ_E for L mode (before polarization) and H mode, with and without inclusion of the polarization power P_E, are shown in the boxes. Data from an OH density ramp (with different wall conditioning) and a family of linear scalings with density are shown for comparison. An increase of 20% appears if the polarization power P_p is not included.

contributing significantly to the plasma energy content. The energy confinement time for TEXTOR OH discharges follows a linear scaling between $\tau_E = 1.1 \times 10^{-21} \bar{n}_{e0} a^{0.8} R_0^{2.3}$ (in seconds) and $\tau_E = 7 \times 10^{-22} \bar{n}_e a R_0^2 q_{cyl}$ with line averaged density as shown in Fig. 14 (squares). The energy confinement times τ_E, obtained for electrode biased discharges including and neglecting the bias power τ_E, are in the range of 40–60 ms and surrounded with boxes in Fig. 14 (this family of polarized discharges features slightly higher confinement times, and follow a slightly better scaling, due to better wall conditioning). The linear scaling is also followed in polarized discharges and thus the increase in energy confinement time observed during polarization (20%) can be explained solely by the density increase resulting from the enhanced particle confinement.

9. The relevance of turbulence driven flux in tokamak plasma

Turbulent particle transport has been commonly identified as the dominant mechanism for radial particle transport [28, 42, 43] across the LCFS, supported by observations that particle confinement and turbulent transport in TEXT [42] and TEXTOR [43] follow the same scaling with various plasma parameters such as density and current. The measured turbulent flux during L mode in our experiments corresponds to τ_p of 29 ms, close to the 35 ms inferred from H_α, and therefore it explains the confinement within error bars. Upon transition to H mode, the turbulent particle flux is reduced by a factor of ∼10–100 at the LCFS, allowing other sources of particle transport to become dominant. We can then evaluate the relative strength of electrostatic turbulence as a source of radial particle transport.

An estimate of the strength of the turbulent transport can be obtained by using the measured τ_p and turbulent particle fluxes. The integral of the total radial particle flux over the LCFS should equal the total number of particles N divided by the particle confinement time τ_p for both the L mode and the H mode condition:

$$\frac{\int \Gamma^L_{total} dA}{\int \Gamma^H_{total} dA} = \frac{N_L \tau_p^H}{N_H \tau_P^L}. \tag{11}$$

From our experiments

$$N_H \approx 1.4 N_L, \quad \tau_p^H \approx 2\tau_p^L$$

and

$$\int \tilde{\Gamma}_r^H dA \approx \frac{1}{10} \int \tilde{\Gamma}_r^L dA \ll \int \Gamma_r^{Other} dA. \tag{12}$$

The total particle flux across the LCFS is a sum of the turbulent $\tilde{\Gamma}_r$ and other (neoclassical, magnetic turbulence induced flux, $\boldsymbol{E} \times \boldsymbol{B}$ convected flux and any other known or unknown sources), dubbed Γ_r^{Other}, particle fluxes integrated over the LCFS. We

will assume that $(\int \Gamma_r^{Other} dA)_L \approx (\int \Gamma_r^{Other} dA)_H$, i.e. the only significant difference in the radial flux between L mode and H mode is the difference in the turbulent flux,

$$\frac{(\int \tilde{\Gamma}_r^L dA) + (\int \Gamma_r^{Other} dA)_L}{(\int \Gamma_r^{Other} dA)_H} = \frac{2}{1.4}$$

$$\Rightarrow F \equiv \frac{\int \tilde{\Gamma}_r^L dA}{(\int \Gamma_r^{Other} dA)_L} \approx 0.42 \qquad (13)$$

F is the ratio of turbulent flux to other fluxes, so it follows that electrostatic turbulence induced transport is nearly 34% of the total flux. Thus, turbulent transport is not the only source, although a dominant one, of transport at the LCFS.

A discussion of how the measured turbulent transport is consistent with the expected sources and total radial fluxes is in order here. Firstly, note that the measured radial turbulent fluxes do not increase with radius (but decrease by a factor of 2–4) over the measured range and secondly note that the flux at the LCFS is enough (if symmetry is assumed) to explain particle confinement. Poloidal variations in turbulent flux, coupled with parallel transport and poloidally asymmetric sources and density profiles, are then required to reconcile the observations. Poloidal variations of the turbulent and quasi-steady-state (or DC) $\boldsymbol{E} \times \boldsymbol{B}$ convected fluxes have been observed in TEXTOR [43, 16] and CCT [44], with the turbulent flux peaking at the outer midplane and waning inboard. These facts, coupled to the observation that poloidal asymmetries exist in the particle sources and in the density profiles in TEXTOR [41], point to a paradigm of edge transport where poloidal asymmetries in radial transport, particle sources and sinks coexist, yet turbulent transport is a dominant channel. A good candidate for an alternative source of particle transport in the edge plasma is the stationary or low frequency convective $\boldsymbol{E} \times \boldsymbol{B}$ flux, which is of the order of the turbulent flux.

10. Conclusions

We have shown that an externally induced positive radial electric field has the effect of reducing turbulence induced radial particle and heat transport, with the larger effects concentrated within the layer of high $\boldsymbol{E} \times \boldsymbol{B}$ shear. The reduction in turbulence induced radial particle transport is mainly due to concomitant changes in the amplitudes of $\tilde{E}_\theta$ and $\tilde{n}$ and a de-phasing of the $\tilde{E}_\theta$ and $\tilde{n}$ fluctuations. The de-phasing is important, resulting in a sign change in the turbulent flux. The reduction in turbulent transport results in a factor of 2 increase on τ_p and translates to a large density gain, suggesting as well that turbulence transport is a dominant mechanism in the edge, yet not the only one. We confirm an increase in τ_E which is due to the density rise via the neo-Alcator dependence of τ_E on density in these ohmic discharges and can therefore be indirectly traced to the increase in particle confinement. The absolute density fluctuation levels and especially the $\tilde{E}_\theta$–$\tilde{n}$ cross-phase show an unexpected dependence on the sign of the velocity shear. The initial local reduction of turbulence levels and de-phasing quickly extends over the edge and SOL and becomes non-localized. The electrostatic turbulent flux in frequency space is suppressed across all measured frequencies, except during the appearance of coherent modes that drive a significant fraction (30–40%) of the remaining transport. It is to be noted that the turbulence and radial particle transport are already affected at modest shear, before the bifurcation in radial conductivity, showing that partial stabilization of turbulence is possible. This result is consistent with the observed pre-bifurcation increase of particle confinement in TEXTOR. Our results thus offer clear evidence of the velocity shear stabilization mechanism and that turbulent particle transport is a dominant loss mechanism in the plasma edge.

Acknowledgements

This work has been supported partially by USDOE Contract No. DE-FG03-85 ER 51069, by the ERM/KMS Brussels and by the IPP, FZ-Jülich. The authors wish to thank K. Burrell for many useful interactions, R. Jaspers for spectroscopy data and acknowledge the support of Prof. P. Vandenplas, Prof. G. Wolf and, especially, L. Russo.

References

[1] ASDEX Team, Nucl. Fusion **29** (1989) 1959.
[2] Taylor, R.J., et al., Phys. Rev. Lett. **63** (1989) 2365.
[3] Moyer, R., et al., Phys. Plasmas **2** (1995) 2397.
[4] Tynan, G.R., et al., Phys. Plasmas **1** (1994) 3301.
[5] Biglari, H., Diamond, P.H., Terry, P.W., Phys. Fluids B **2** (1990) 1.
[6] Ritz, C.P., et al., Phys. Rev. Lett. **65** (1990) 2543.
[7] Burrell, K.H., et al., Plasma Phys. Control. Fusion **34** (1992) 1859.
[8] Burrell, K.H., et al., Phys. Plasmas **1** (1994) 1536.

[9] Synakowski, E.J., et al., Phys. Plasmas **4** (1997) 1736.
[10] Synakowski, E.J., et al., Phys. Rev. Lett. **78** (1997) 2972.
[11] Weynants, R.R., Jachmich, S., Van Oost, G., Plasma Phys. Control. Fusion **40** (1998) 635.
[12] Weynants, R.R., et al., Nucl. Fusion **32** (1992) 837.
[13] Cornelis, J., et al., Nucl. Fusion **34** (1994) 171.
[14] Weynants, R.R., et al., in Plasma Physics and Controlled Nuclear Fusion Research 1990 (Proc. 13th Int. Conf. Washington, DC, 1990), Vol. 1, IAEA, Vienna (1991) 473.
[15] Jachmich, S., et al., Plasma Phys. Control. Fusion **40** (1997) 1105.
[16] Tynan, G.R., et al., J. Nucl. Mater. **196–198** (1992) 770.
[17] Waltz, R.E., et al., Phys. Plasmas **2** (1995) 2408.
[18] Wang, X.H., Diamond, P.H., Rosenbluth, M.N., Phys. Fluids B **4** (1992) 2402.
[19] Shaing, K.C., Crume, E.C., Houlberg, W.A., Phys. Fluids B **2** (1990) 1492.
[20] Itoh, K., Itoh, S., Phys. Plasmas Control. Fusion **38** (1996) 1.
[21] Burrell, K.H., Phys. Plasmas **4** (1997) 1499.
[22] Hahm, T.S., Burrell, K.H., Phys. Plasmas **2** (1995) 1648.
[23] Zohm, H., et al., Plasma Phys. Control. Fusion **36** (1994) A129.
[24] Goebel, D.M., et al., J. Nucl. Mater. **162–164** (1989) 115.
[25] Boedo, D., et al., Rev. Sci. Instrum. **69** (1998) 2663.
[26] Bickerton, R.J., Nucl. Fusion **13** (1973) 290.
[27] Ware, A.S., et al., Plasma Phys. Control. Fusion **38** (1990) 1343.
[28] Moyer, R.A., et al., J. Nucl. Mater. **196–198** (1992) 854.
[29] Powers, E.J., Nucl. Fusion **14** (1974) 749.
[30] Ross, D.W., Comments Plasma Phys. Control. Fusion **12** (1989) 155.
[31] Boedo, J., et al., Phys. Rev. Lett. (in press).
[32] Ritz, C., et al., Phys. Rev. Lett. **62** (1989) 1844.
[33] Lin, H., Bengtson, R.D., Ritz, C.P., Phys. Fluids **1** (1989) 2027.
[34] Stoneking, M.R., Lanier, N.E., Prager, S.C., Sarff, J.S., Sinitsys, D., Phys. Plasmas **4** (1997) 1632.
[35] Beall, J.M., et al., J. Appl. Phys. **53** (1982) 3933.
[36] Ware, A.S., Terry, P., Diamond, P., Carreras, B., Plasma Phys. Control. Fusion **38** (1990) 1343.
[37] Carreras, B.A., Lynch, V.E., Garcia, L., Diamond, P.H., Phys. Plasmas **2** (1995) 2744.
[38] Staebler, G.M., Dominguez, R.R., Nucl. Fusion **31** (1991) 1891.
[39] Dominguez, R.R., Staebler, G.M., Phys. Fluids B **5** (1993) 3876.
[40] Diamond, P.H., et al., in Plasma Physics and Controlled Nuclear Fusion Research 1992 (Proc. 14th Int. Conf. Würzburg, 1992), Vol. 2, IAEA, Vienna (1993) 97.
[41] Gray, D., et al., Nucl. Fusion **38** (1998) 1585.
[42] Rowan, W.L., et al., Nucl. Fusion **27** (1987) 1105.
[43] Boedo, J., et al., in Controlled Fusion and Plasma Physics (Proc. 22nd Eur. Conf. Bournemouth 1995), Vol. 19C, Part I, European Physical Society, Geneva (1995) 293.
[44] Tynan, G.R., et al., Phys. Rev. Lett. **68** (1992) 3032.

(Manuscript received 27 April 1998
Final manuscript accepted 21 March 2000)

E-mail address of J. Boedo: boedo@fusion.gat.com

Subject classification: D2, Te; E0, Te; F2, Te; I1, Te